Chapter 2
Experimental Characterization of Fiber-Reinforced Composite Materials

2.1 Introduction

The anisotropic nature of fiber-reinforced composite materials makes their experimental characterization a complicated task. In general, composites exhibit different properties under tension and compression, under both quasi-static and fatigue loading patterns. The increased number of parameters that affect the material properties, such as loading rate, temperature and humidity, mean stress and load frequency, necessitate the careful and targeted design of an experimental program for the characterization of a composite material in order to use it for a specific application, since it is theoretically impossible to take into account all the parameters and simulate their effect on material behavior. This characteristic of composite materials makes their incorporation in design codes and guidelines difficult.

For the design of a structure based on the static strength or stiffness there are a number of available theories in the literature. It is up to the design engineer to select the failure criterion that fits the requirements of each application and matches the nature of the selected material. However, the criterion selection can be validated only after comparison of the theoretical predictions with some experimental data. It should also be mentioned that the most appropriate criterion for the prediction of material behavior under a given loading pattern can present disadvantages when another material is examined or even for the same material but under different loading conditions.

For fatigue loading, the situation is much more complicated since the material properties change during loading. This difficulty is increased by the fact that this property variation (normally degradation) is not linear since its rate depends on the loading conditions and material status, i.e. how far it is from failure. In general, the inability to accurately model material behavior leads to the adoption of high coefficients of safety, which, in addition to those already used due to the stochastic nature of the fatigue loading leads to the over dimensioning of each structure. It is

therefore necessary to be able to characterize each material and appropriately model its quasi-static and fatigue behavior in order to develop theories that will assist the design process.

The fatigue behavior of carbon fiber-reinforced plastics (CFRP) has been extensively investigated over the last 40 years thanks to the concentrated effort to develop composite structural components for aeronautical applications. Most aspects of fatigue-related engineering problems, i.e. life prediction, property degradation, joint design etc., were addressed, leading to the adoption of design allowables and the production of a large amount of published data, e.g. [1–5]. However, damage tolerance issues have not been efficiently dealt with [6] for many reasons, the main one being the lack of definition of a generalized damage metric, such as the crack length in metals, that could be used with different lay-ups and material configurations [7]. In addition, the effect of variable amplitude loading on the remaining life and the fatigue behavior of composite materials under complex stress states have only received limited attention.

The structural response to cyclic loads of glass fiber-reinforced plastics (GFRP), extensively used in a number of engineering applications such as leisure boats, transportation, wind turbine rotor blades, helicopter rotor blades and bridge decks, was not investigated to any significant extent until 25 years ago. Due to the amazing growth of the wind energy industry, especially in Europe, much effort has been devoted during the last two decades to establishing fatigue design allowables for GFRP, in particular laminated composites for wind turbine rotor blades. A great deal of experimental data was produced characterizing the fatigue strength of matrix systems such as polyester, epoxies and vinylester reinforced by continuous glass fibers in the form of woven or stitched fabrics and unidirectional roving [8–17]. The effect of both constant and variable amplitude, i.e. spectral loading conditions, was investigated.

However, limited experimental data and design guidelines addressing the complex stress state effect on the fatigue behavior of GFRP laminates have been produced by applying either multiaxial or off-axis loading. Studies [18–22] point out the strong dependency of fatigue response on load direction, as a result of material anisotropy, and indicate the need to continue research in this domain, including the effects of spectral and non-proportional loading.

Typical modern composite structures such as aeronautical vehicles and wind turbine rotor blades are subjected to severe dynamic loads of stochastic and deterministic nature. The stress state in their primary structural elements, in the form of thin and moderately thick shells made of laminated fiber-reinforced polymers, can be assumed plane, i.e. composed of two normal components and an in-plane shear component of the stress tensor. A formidable task for designers is the life prediction of such components subjected to irregular stress histories caused by multiaxial loads of variable amplitude. There are many critical decisions that should be made related to this issue that concern both the experimental characterization of relevant mechanical material properties and the establishment of reliable life prediction methods.

In the case of laminated FRP materials, mechanical properties, i.e. elasticity, strength and hygro-thermal property tensors, can be measured for the entire laminate as a homogeneous anisotropic medium, an approach known as "direct characterization". Alternatively, mechanical properties can be measured for each individual layer and then theoretical methods can be used to predict the laminate behavior. There are advantages and disadvantages to both approaches. In the former, results are valid only for the specific lay-up and cannot be used in a laminate optimization design algorithm. In addition, for asymmetric or unbalanced stacking sequences, there are property couplings that cannot be measured appropriately. The latter approach, "ply-to-laminate characterization", although successfully implemented for elastic and hygro-thermal properties, remains an unresolved issue concerning the strength prediction of laminated composites due to difficulties of modeling damage progression and interaction effects. The situation is even more complicated in the case of fatigue strength and life prediction.

Systematic research efforts regarding the fatigue property characterization of GFRP composites have led to the development of magnificent fatigue databases during the last two decades and the establishment of reliable life prediction methodologies [9–16, 20–23]. However, all these experimental investigations focused mainly on the axial property characterization of various laminates, i.e. direct characterization in only one direction of an anisotropic medium. Therefore, this effort and the accumulated experimental results, including constant (CA) and variable amplitude (VA) loading, have limited use when life prediction under irregular, multidimensional stress histories is required.

Experimental results are presented here from a comprehensive program consisting of quasi-static and fatigue tests on straight edge specimens cut at various on- and off-axis directions from a GFRP multidirectional (MD) laminate of $[0/(45)_2/0]_T$ lay-up. The fatigue behavior of off-axis loaded laminates, i.e. complex state of stress in material principal directions, is investigated in depth for several off-axis orientations. This includes the derivation of S–N curves at various R-ratios ($R = \sigma_{min}/\sigma_{max}$), statistical evaluation of fatigue strength results and determination of design allowables at specific reliability levels. Constant life diagrams are extracted for the various off-axis directions and compared with existing data from similar material systems.

2.2 Experimental Program

2.2.1 Structural Fiber-Reinforced Composite Materials: Multidirectional Laminates

The material system was E-glass/polyester, with the E-glass being supplied by Ahlstrom Glassfibre, and the polyester resin, Chempol 80 THIX, by Interchem. This resin is a thixotropic unsaturated polyester and was mixed with 0.4% cobalt
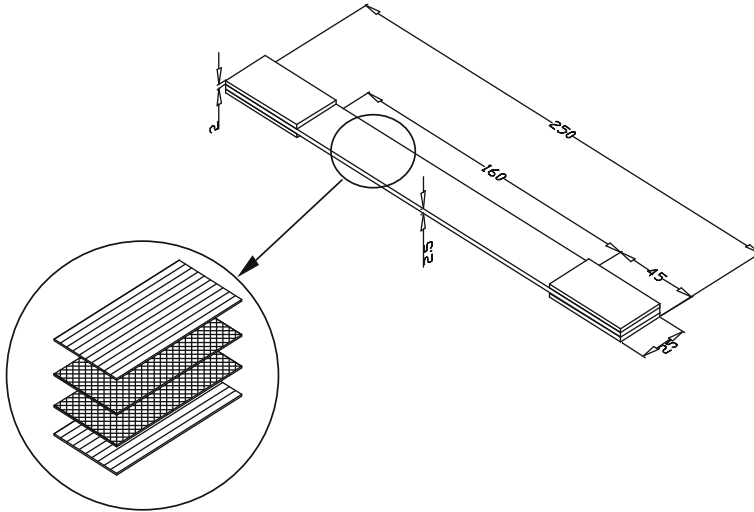
Fig. 2.1 Specimen geometry and stacking sequence. Specimen cut at 90° off-axis is shown

naphthenate solution (6% Co) accelerator and 1.5% methyl ethyl ketone peroxide, MEKP (50% solution) catalyst. A systematic experimental investigation was undertaken, consisting of static and fatigue tests on straight edge specimens cut at various directions from a multidirectional laminate. The stacking sequence of the E-glass/polyester plate consisted of four layers, 2 UD, unidirectional lamina of 100% aligned warp fibers, with a weight of 700 g/m^2 as outer layers and 2 stitched laminae with fibers along $\pm 45^\circ$ directions, of 450, 225 g/m^2 in each off-axis angle.

Rectangular plates were fabricated using a hand lay-up technique and cured at room temperature. Considering the UD layer fibers as being along the 0° direction, the lay-up can be encoded as $[0/(\ 45)_2/0]_T$. Specimens were cut using a diamond wheel at 0°, on-axis, and 15°, 30°, 45°, 60°, 75° and 90° off-axis directions.

The specimens were prepared according to the ASTM 3039/D3039 standard, their edges were trimmed with sandpaper and aluminum tabs were glued at their ends. The specimens were 250 mm long and had a width of 25 mm. Their nominal thickness was 2.6 mm. The length of the tabs, with a thickness of 2 mm, was 45 mm leaving a gauge length of 160 mm for each of the specimens. The specimen dimensions are shown in Fig. 2.1.

Quasi-static and fatigue experiments were performed on the total number of 355 specimens as follows: 31 specimens for static tests to provide baseline data, with both tensile and compressive strengths being obtained, while 277 specimens were tested under uniaxial cyclic stress of constant amplitude for the determination of 17 S–N curves at various off-axis directions and loading conditions and the investigation of the effect of the load interruption on the fatigue life. Additionally, 47 specimens were tested under two different variable amplitude spectra, a modified version of the WISPERX used in the wind turbine rotor blade industry, and a realistic irregular fatigue spectrum derived from aeroelastic calculations.

Table 2.1 Failure stresses of examined material system

	UTS (MPa)		UCS (MPa)	
	Mean value	S.D.	Mean value	S.D.
	Displacement control, 1 mm/min			
0°	244.84 (4)	18.08	216.68 (4)	14.67
30°	130.52 (2)	14.23	145.52 (2)	13.94
45°	139.12 (2)	25.61	106.40 (2)	2.69
60°	117.26 (2)	16.64	99.52 (2)	3.59
90°	84.94 (3)	2.06	83.64 (3)	5.37
Shear	61.38 = (139.12 + 106.40)/2/2			
	Load control, 40 kN/s			
0°	417.49 (5)	74.86		

2.2.2 Quasi-Static Experiments: Off-Axis Strength Prediction

Tensile and compressive experiments were performed for the derivation of the strength of the examined material. The majority of the experiments were performed under displacement-control mode (1 mm/min), while a limited number of tensile experiments on specimens cut at $0°$ were performed under load-control mode with a loading rate of 40 kN/s, much faster than the corresponding loading rate in the displacement-controlled experiments. The results are presented in Table 2.1. The failure stress obtained from the load-controlled experiments was 417.49 MPa, approximately 1.7 times the corresponding strength of 244.84 MPa obtained in the relatively slow, displacement-controlled experiments. This result proves the significant effect of the loading rate on the strength of the examined polymer matrix material.

The symbols X, X', Y and Y' will be used in the following to denote the tensile and compressive strengths along the longitudinal (X) and transverse (Y) material directions. The shear strength is represented by S and is considered to be the same under positive or negative shear stresses, according to the sign convention, a hypothesis that has been experimentally validated in the past and is assumed safe for technical applications and shear strengths along the principal planes of orthotropic media or media with higher symmetry.

The static strengths of the material along different directions are presented in Fig. 2.2. Theoretical predictions provided by the Failure Tensor Polynomial (FTP) quadratic failure criterion [24] are also shown in this figure by a solid line. The form of the failure criterion used is:

$$\frac{\sigma_1^2}{XX'} + \frac{\sigma_2^2}{YY'} - \frac{\sigma_1\sigma_2}{XY} + \sigma_1\left(\frac{1}{X} - \frac{1}{X'}\right) + \sigma_2\left(\frac{1}{Y} - \frac{1}{Y'}\right) + \frac{\sigma_6^2}{S^2} - 1 = 0 \qquad (2.1)$$

where the Tsai-Hahn version of the quadratic failure criterion was used with the interaction term taking the form:

$$F_{12} = -0.5\sqrt{F_{11}F_{12}} \qquad (2.2)$$

Fig. 2.2 Off-axis static
strength of examined GFRP
laminate
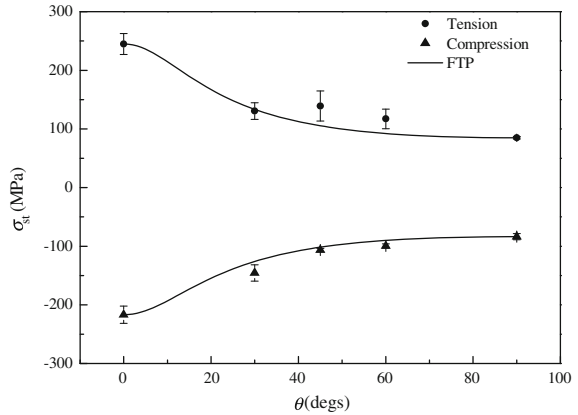
and the shear strength is considered equal to half of the tensile strength of spec-
imens cut at 45° off-axis, as presented in Table 2.1.

With σ_i, $i = 1$, 2, 6 denoting the in-plane stress tensor components in the
principal coordinate system (PCS) of the multidirectional laminate and σ_x the
applied normal stress at an off-axis angle , the following transformation equation is
valid:

$$\sigma_1 = \sigma_x \cos^2 \theta$$
$$\sigma_2 = \sigma_x \sin^2 \theta \qquad (2.3)$$
$$\sigma_6 = \sigma_x \sin \theta \cos \theta$$

The strength of the material along each off-axis angle direction can be
calculated by replacing the stresses σ_1, σ_2 and σ_6 in Eq. 2.1 and solving it
for σ_x.

The static strength under both tension and compression was the highest for
the 0° MD specimens, while is considerably and continuously decreased with
higher off-axis angles. The peculiar behavior of the 45° specimens, exhibiting
higher static strength than the 30° specimens, was to be expected and was related
to the stacking sequence of the laminate under consideration. When specimens
are cut at 45°, the fibers of the stitched (±45) layers become on-axis and the
prevailing failure mode shifts from matrix-dominated, observed in 30° and 60°
off-axis specimens, to partially fiber-controlled. Therefore, these fibers bear most
of the load instead of the matrix. This effect was not observed under compressive
loads since in that case the matrix is the dominant component and therefore
fibers of the ±45 layers do not significantly contribute to the strength of the
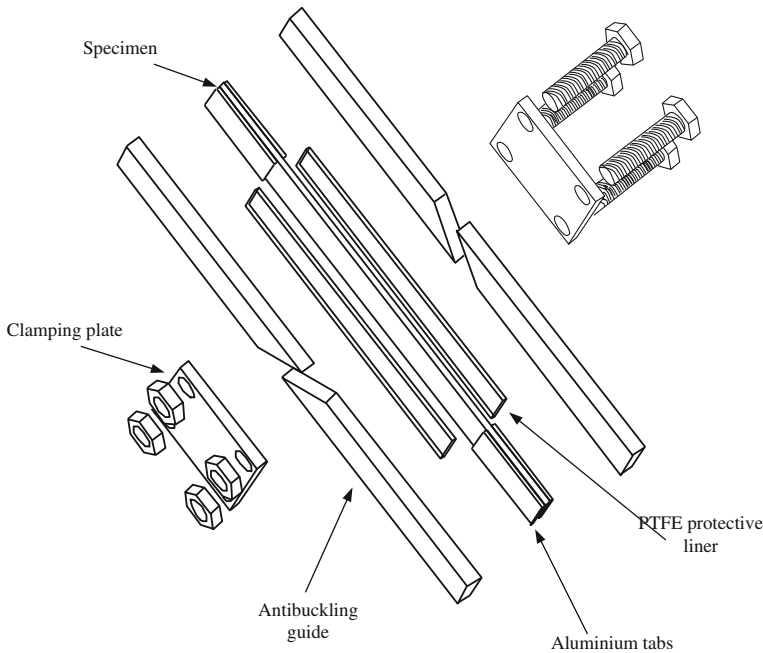material. In general, a mixed failure mode was observed for all the off-axis
specimens.

Fig. 2.3 Antibuckling device

2.2.3 Fatigue Experiments: Derivation of S–N Curves

Cyclic experiments of sinusoidal waveform and constant amplitude were also carried out in the same machine under load control. In total, 17 S–N curves were determined experimentally along various off-axis loading directions, under four different stress ratios, namely, $R = 10$ representing compression-compression loading (C-C), $R = -1$ representing tension-compression reversed loading (T-C) and $R = 0.1$ and $R = 0.5$ representing tension-tension fatigue loading (T-T). The frequency was kept constant at 10 Hz for all the tests as no appreciable temperature increase was detected during cycling under various loading conditions.

Loading was continued until specimen ultimate failure or 10^6 cycles, whichever occurred first. In particular, for the on-axis specimens, $0°$, under reversed loading, $R = -1$, loading was continued for up to 5×10^6 cycles. Specimens that did not fail, and were removed after a specific number of cycles were marked as "run-outs". For all the tests with compressive cycles, the antibuckling device shown in Fig. 2.3 was used. At least three specimens were tested at each one of the four or five stress levels. All tests were conducted at room temperature, 18°–22°C.

Uniaxial tests on specimens cut off-axis from principal material directions were performed to induce complex stress states in the principal coordinate system (PCS), according to Eq. 2.3. The biaxiality ratios σ_2/σ_1 and σ_6/σ_1 as a function of take values equal to $\tan^2\theta$ and $\tan\theta$, respectively.

Fig. 2.4 Fatigue data and S–N curves for $R = 10$
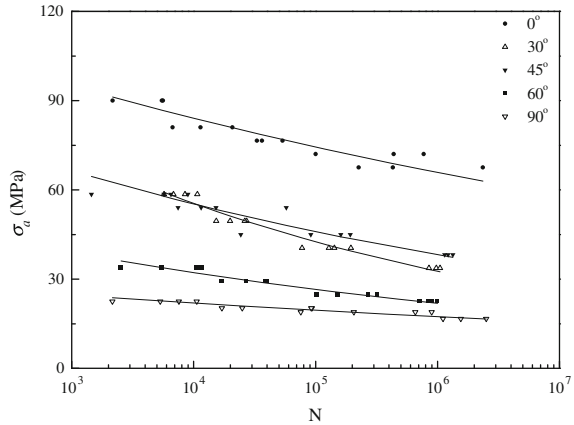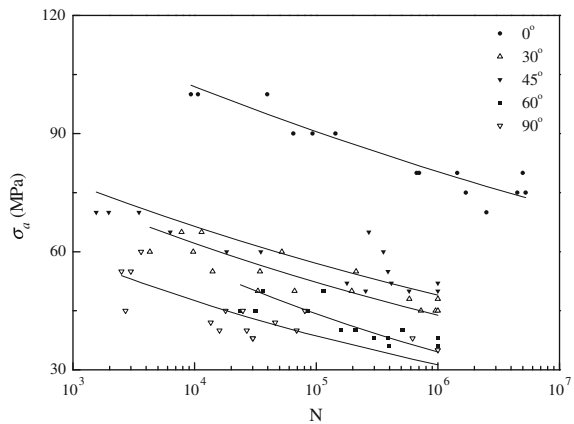

Fig. 2.5 Fatigue data and S–N curves for $R = -1$

The results of the fatigue testing are presented in Figs. 2.4, 2.5, 2.6, and 2.7. Traditionally, constant amplitude fatigue data are plotted on the S–N plane. The number of cycles to failure is plotted on the abscissa, and the stress parameter on the ordinate. However, as mentioned in ASTM E739-91 (2004), the stress level must be considered as the independent variable, whereas the corresponding number of cycles to failure must be the dependent one. This is how the fatigue data have been used here for estimation of the derived S–N curve parameters.

Typical fitted lines of the form:

$$\sigma_a = \sigma_o N^{-\frac{1}{k}} \qquad (2.4)$$

are also plotted together with the fatigue data. The coefficients σ_o and k are given in Table 2.2. The detailed fatigue data are given in Tables 2.3, 2.4, 2.5, and 2.6.

Conclusions concerning the fatigue behavior of the examined material can be derived from observation of these figures. Off-axis fatigue strengths follow the same trend as the corresponding static ones. Figure 2.4 for the reversed loading

Fig. 2.6 Fatigue data and
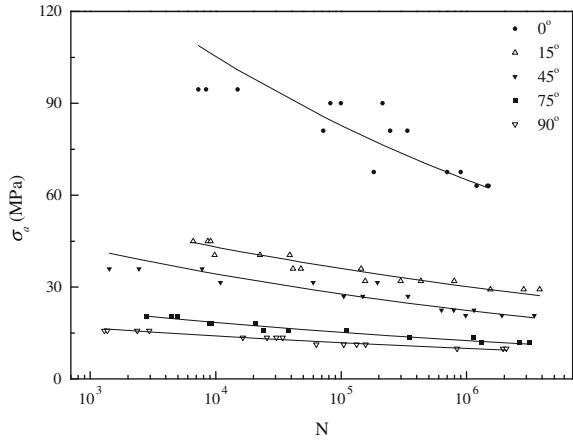S–N curves for $R = 0.1$
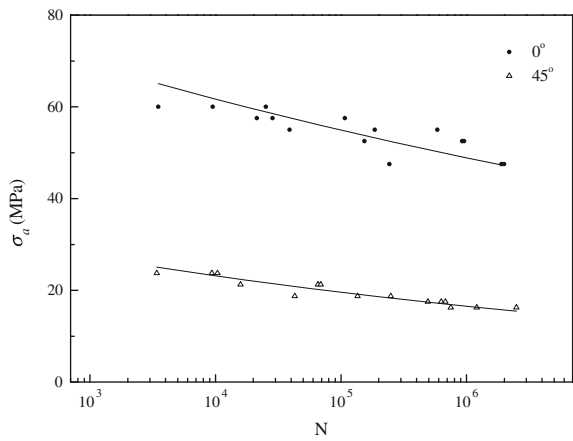

Fig. 2.7 Fatigue data and
S–N curves for $R = 0.5$

Table 2.2 Estimated model parameters for the on- and off-axis specimens. Equation of the form:
$\sigma_a = \sigma_o N^{-\frac{1}{k}}$

R-ratio Off-axis angle	10		−1		0.1		0.5	
	σ_o (MPa)	1/k	σ_o (MPa)	1/k	σ_o (MPa)	1/k	σ_o (MPa)	1/k
0°	137.13	0.0531	164.10	0.0517	276.16	0.1047	98.22	0.0505
15°					88.02	0.0775		
30°	159.91	0.1150	124.54	0.0755				
45°	115.68	0.0802	122.26	0.0662	80.27	0.0924	45.46	0.0732
60°	69.92	0.0842	152.67	0.1076				
75°					39.89	0.0838		
90°	35.22	0.0512	109.95	0.0910	27.98	0.0749		

Table 2.3 Number of cycles to failure of specimens cut at different on- and off-axis angles and tested under $R = 10$

σ_a (MPa)	σ_{max} (MPa)	0°	30°	45°	60°	90°
90	200	5,500; 2,161; 5,607				
81	180	20,776; 11,400; 6,728				
76.5	170	53,626; 33,052; 36,350				
72	160	770,046; 437,115; 100,184				
65.5	150	2,357,018; 431,315; 225,912				
58.5	130		6,819; 5,713; 8,500; 10,727	5,716; 8,972; 1,453; 6,519		
54	120			7,465; 15,257; 11,500; 57,500		
49.5	110		27,173; 26,292; 19,888; 15,329			
45	100			91,597; 25,317; 192,288; 161,427		
40.5	90		128,527; 195,000; 77,433; 142,397			
38.25	85			1,145,696; 1,338,602; 1,221,080		
33.75	75		850,000; 976,497; 1,050,000		11,675; 5,442; 10,545; 2,540	
29.25	65				16,943; 38,911; 26,841; 40,316	
24.75	55				150,000; 270,000; 317,000; 102,412	

Table 2.3 (continued)

σ_a (MPa)	σ_{max} (MPa)	0°	30°	45°	60°	90°
22.5	50				710,316; 840,316; 896,316; 1,000,000 →	5,316; 2,158; 7,567; 10,595
20.25	45					93,315; 17,042; 92,141; 25,006
18.9	42					75,724; 896,052; 206,244; 658,432
16.65	37					1,111,693; 2,505,659; 1,554,429

(:→Run-out)

shows that the fatigue strength of the material at 45° is superior to the fatigue strength at 30°, which is in line with the static case and is attributed to the same reason, the presence of fibers along the 45° and −45° directions in the multidirectional laminate.

The slopes of the derived S–N curves have values that range between 0.05 and 0.12, in agreement with corresponding values in the literature for other GFRP systems, e.g. [25, 26]. For the on-axis specimens it is shown that the material is more sensitive to tensile fatigue loading patterns than to compressive ones.

2.2.4 Mean-Stress Effect

Comparison of the S–N curves for different R-ratios, see Figs. 2.8, 2.9, and 2.10, shows different behavior between the on- and off-axis specimens. For the on-axis specimens that fail due to the eventual failure of the fibers, it is shown (Fig. 2.8) that when fatigue life is plotted against the maximum cyclic stress, σ_{max}, the reversed loading is the worst case, with the tensile fatigue loading being the least critical, especially for low numbers of fatigue cycles, less than 800,000 in this case. This observation is in line with the quasi–static behavior of the material, which is stronger under tension than under compression. However, the accumulation of matrix cracks during loading that is more pronounced for the tensile loading (see following paragraphs) gradually reduces the fatigue strength of the material and therefore the S–N curve for $R = 0.1$ is steeper than the corresponding one for $R = 10$. The same comment (the reversed loading is the most critical) applies for the specimen cut at 45° from the multidirectional laminates, see Fig. 2.9, although

Table 2.4 Number of cycles to failure of specimens cut at different on- and off-axis angles and tested under $R = -1$

σ_a (MPa)	σ_{max} (MPa)	0°	30°	45°	60°	90°
100	100	10,700; 39,637; 9,350				
90	90	64,871; 93,498; 143,896				
80	80	670,275; 702,056; 1,446,527; 5,000,000→				
75	75	4,500,000→ 1,700,786; 5,269,524				
70	70			1,557; 3,500; 1,972		
65	65		7,820; 11,407	6,317; 270,633		
60	60		4,298; 52,316; 9,749	18,375; 357,155; 35,012		
55	55		14,098; 34,538; 212,856			3,641; 2,510; 3,000
52	52			179,000; 415,000; 1,000,000		
50	50		195,710; 33,149; 66,559	255,000; 580,995; 1,000,000→	36,774; 115,000	
48	48		581,997; 1,000,000			
45	45		956,933; 726,537; 1,000,000→		85,700; 32,000; 23,769	2,700; 18,000; 80,556; 25,000
42	42					29,850; 13,580; 46,120
40	40				209,560; 512,000; 161,000	26,916; 69,134; 16,027
38	38				388,000; 298,317; 1,000,000→	70,030; 30,206; 620,305
36	36				395,000; 1,000,000→ ; 1,007,000	
35	35					1,000,000; 1,000,000→

(:→Run-out)

in this case the S–N curve for tensile loading is significantly lower than that derived under $R = 10$. However, for specimens cut at 90°, the most critical loading pattern seems to be the tensile one, $R = 0.1$, see Fig. 2.10. The lack of fibers along the loading direction, which makes the material vulnerable to tensile loads, is the

Table 2.5 Number of cycles to failure of specimens cut at different on- and off-axis angles and tested under $R = 0.1$

σ_a (MPa)	σ_{max} (MPa)	0°	30°	45°	60°	90°
94.5	210	8,400; 7,284; 15,000				
90	200	82,000; 214,300; 99,783				
81	180	337,760; 245,995; 72,100				
67.5	150	898,645; 701,093; 182,123				
63	140	1,204,333; 1,464,000; 1,500,000				
45	100		9,125; 6,610; 8,654			
40.5	90		22,613; 9,834; 38,891			
36	80		41,330; 144,730; 47,894	7,819; 2,450; 1,420		
31.5	70			10,935; 59,821; 195,116		
31.95	71		298,233; 155,864; 432,283; 798,467			
29.25	65		3,828,947; 2,852,760; 1,549,331			
27	60			149,100; 105,000; 342,000		
22.5	50			793,000; 1,150,000; 632,089		
20.7	46			985,000; 1,915,000; 3,462,000		
20.25	45				4,419; 2,815; 4,965	
18	40				9,226; 20,715; 8,924	

Table 2.5 (continued)

σ_a (MPa)	σ_{max} (MPa)	0°	30°	45°	60°	90°
15.75	35				111,152; 38,237; 24,111	1,296; 2,954; 2,370; 1,370
13.5	30				1,149,039; 354,521; 354,109	30,441; 25,581; 16,440; 34,181
11.7	26				1,325,554; 2,654,235; 3,200,000	
11.25	25					133,043; 104,913; 156,936; 63,520
9.9	22					839,958; 1,955,673; 2,075,673

Table 2.6 Number of cycles to failure of specimens cut at different on- and off-axis angles and tested under $R = 0.5$

σ_a (MPa)	σ_{max} (MPa)	0°	45°
60	240	25,210; 9,500; 3,500	
57.5	230	107,441; 28,461; 21,333	
55	220	38,970; 586,000; 185,694	
52.5	210	923,020; 956,833; 154,000	
47.5	190	1,996,000; 243,500; 1,900,000	
23.75	95		3,411; 9,370; 10,393
21.25	85		65,459; 15,858; 68,947
18.75	75		42,900; 135,872; 249,194
17.5	70		630,000; 493,345; 678,643
16.25	65		1,208,000; 750,000; 2,500,000→

(:→Run-out)

reason for this phenomenon. Although under quasi–static loading the 90° specimens exhibit almost identical strengths, the damage done to the material in the form of matrix cracking proved critical in the case of fatigue loading.

Similar conclusions are reported in other experimental works. In [25] it is mentioned that in multidirectional composite laminates with layers at 0° and 45°, with a stacking sequence of [0/±45/0]$_S$, the reversed loading is the most detrimental for the fatigue life since the strain-life (ε-N) curve for this case is lower

Fig. 2.8 S–N curves for
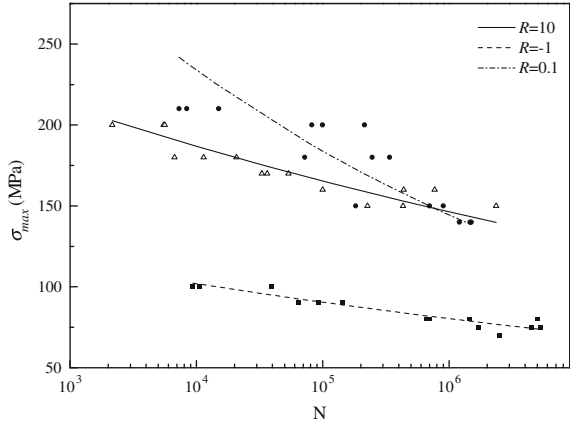different *R*-ratios. On-axis
specimens

Fig. 2.9 S–N curves for
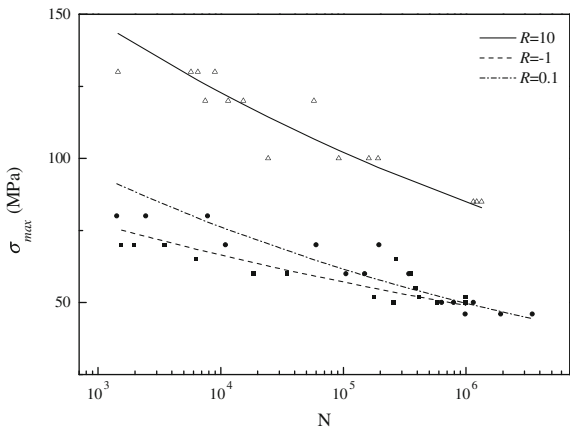different *R*-ratios. 45° off-axis
specimens

Fig. 2.10 S–N curves for
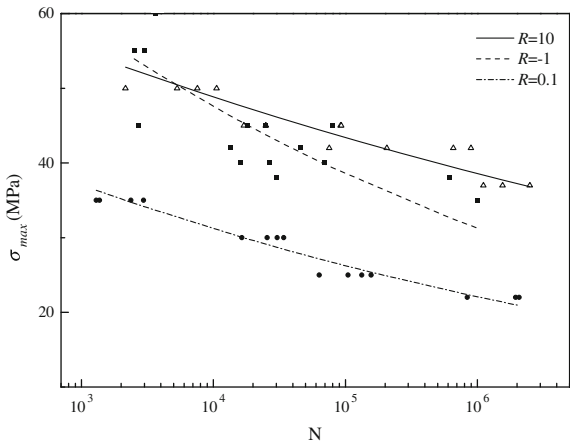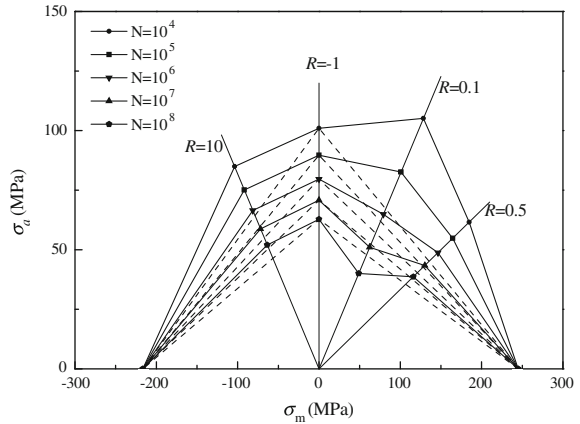different *R*-ratios. Specimens
cut at 90°

than the corresponding one under tensile fatigue loading of $R = 0.1$. Experiments under block loading conditions on CFRP composite laminates were reported in [26]. The authors concluded that the combination of tensile and compressive loading is more critical for the fatigue life than tensile or compressive loading alone. Results from a benchmarking program carried out by several laboratories are reported in [9]. It is demonstrated that for composite materials with the majority of the fibers along the loading direction, reversed loading causes earlier failure than other fatigue loading patterns.

Other materials, such as wood, exhibit analogous behavior. Results from an experimental program on epoxy resin specimens reinforced by different types of wood [27] showed that the fatigue life under $R = -1$ is the shortest compared to the life under different R-ratios. The specimens tested under tensile loads exhibited the longest lives.

The effect of mean stress on the fatigue life of the examined composite laminates can be easily visualized using the constant life diagrams. For the derivation of a constant life diagram, the fatigue data are normally plotted on the $(\sigma_m$–$\sigma_a)$-plane as radial lines emanating from the origin of the coordination system. Each line represents a single S–N curve at a given R-ratio and can be reproduced using the following equation:

$$\sigma_a = \left(\frac{1-R}{1+R}\right)\sigma_m \tag{2.5}$$

Constant life lines can be derived by joining in a linear or non-linear way the points on each S–N curve (radial line) corresponding to the same number of cycles. Several methods have been proposed for the derivation of a CLD, see Chap. 4.

For the examined material the constant life diagrams for the on-axis and 45° and 90° off-axis specimens are presented in Figs. 2.11, 2.12, and 2.13. For the specimens cut on-axis and those cut at 45°, four S–N curves have been

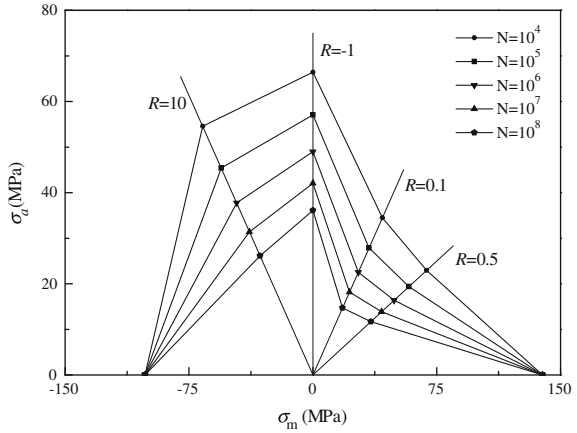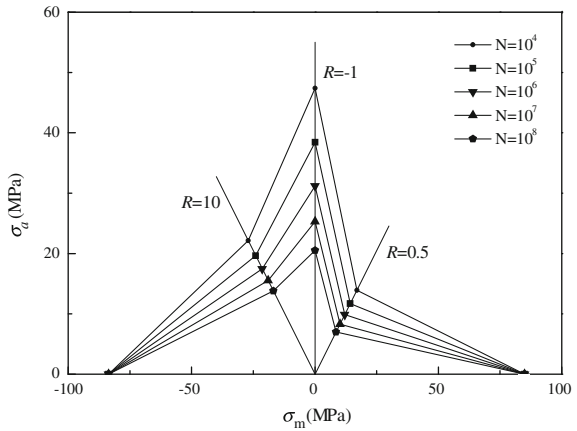**Fig. 2.12** Constant life diagram for 10^4–10^8 loading cycles, 45° off-axis specimens

**Fig. 2.13** Constant life diagram for 10^4–10^8 loading cycles, 90° off-axis specimens

experimentally derived, under $R = 10$, –1, 0.1 and 0.5, while three, under $R = 10$, –1 and 0.1, are available for the 90° specimens.

It is obvious that for the on-axis specimens (Fig. 2.11) the constant life lines follow a Gerber line rather than the linear Goodman relationship. Therefore it is expected that the use of the Goodman diagram (shown by dashed lines in Fig. 2.11) as proposed in several design codes for structures made of composite materials, would lead to a very conservative design. Another interesting conclusion is that the material seems to be more fatigue resistant against compressive fatigue loads for the high cycle fatigue range, while the opposite holds true for small cycle numbers. This observation has also been mentioned by other researchers [14] for a similar GFRP material system, see Fig. 2.14. It is worth mentioning that in this case, even the linear Goodman relationship is less conservative compared to the experimental data for lives beyond 10^7.

The experimental results for the off-axis specimen are representative of the anisotropy of the examined material, since as presented the behavior is extremely

Fig. 2.14 Constant life diagram for 10^4–10^8 loading cycles. GL/P specimen with fibers at 0/90/45 directions [11]
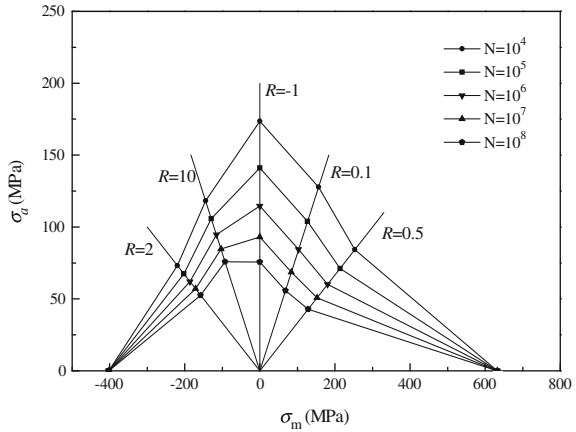
different from that referred to above for the on-axis specimens. For the off-axis specimens it is observed that the fatigue strength under compressive loading is superior to the tensile fatigue strength, as was also explained above. Furthermore, it is obvious that the linear Goodman relation cannot, in most cases, describe fatigue behavior accurately.

2.2.5 Interrupted Constant Amplitude Fatigue Loading

Although the described experimental program assists the derivation of fatigue design allowables, it does not deal with the subject of interrupted cyclic loading. As is well known, engineering structures do not operate continuously, but their operation is interrupted for several reasons, e.g. airplanes taking off, flying and landing, and then rest until the next flight, or wind turbines that stop when wind speed exceeds the limit of 25 m/s etc. It could thus be disputed whether or not the fatigue design allowables determined under continuous loading patterns are valid to accurately describe the fatigue behavior of composite materials and structures.

The influence of load interruption on fatigue life is examined here. Specimens cut from the same GFRP laminates at $0°$ direction were loaded at a single stress level under tension-tension ($R = 0.1$) fatigue loads until failure. Other specimens were loaded under the same conditions, but the loading was interrupted after a predetermined number of cycles. It was found that life was increased by a factor of 1.4 for this particular stress level.

Compared to experimental results from the aforementioned experimental program, it is shown that results from continuously loaded specimens fall within the experimental scatter of the S–N curve derived for $0°$ specimens, under $R = 0.1$. However, experimental results from specimens that were not loaded continuously could belong to another S–N curve, corresponding to longer fatigue life.

Table 2.7 Fatigue life of on-axis specimens under continuous and interrupted loading conditions

Specimen	Number of cycles to failure continuous loading	Number of cycles to failure Interrupted loading
1	51,316	242,546
2	42,163	203,629
3	150,319	64,050
4	86,197	296,903
5	400,316	268,345
6	57,460	209,279
7	550,316	187,598
8	87,280	63,397
9	58,963	379,900

The maximum applied load was maintained constant for all specimens at 11.1 kN, which corresponds to a maximum cyclic stress level of approximately $\sigma_{max} = 185$ MPa, according to each specimen's actual geometry. According to previous experimental data for the same material configuration, under the same test conditions, the allowable number of cycles for this cyclic stress level is approximately 200,000.

Half of the twenty specimens used in this short experimental program were loaded continuously until failure, and load reversals were recorded. The rest of the specimens were loaded for 5,000 cycles, and then left to rest for at least 1 h before resuming the test for another set of 5,000 cycles and so on until their failure. The total number of cycles until failure was also recorded for this type of test. Of the 20 fatigue tests conducted, 18 were considered valid, as one test from each group was rejected because of unacceptable failure mode; specimens failed in the tabs after a few cycles of loading. The fatigue life for the rest of the specimens is given in Table 2.7.

Assuming that the test data of each group follow a two-parameter Weibull distribution with a probability of survival:

$$P_S(N) = \exp\left[-\left(\frac{N}{N_o}\right)^{\alpha_f}\right] \tag{2.6}$$

The scale and shape parameters for the two distributions were estimated with MLE as $N_{ocont} = 170{,}790$ cycles and $\sigma_{fcont} = 1.08$, for continuous loading and $N_{oint} = 239{,}977$ cycles and $\sigma_{fint} = 2.37$ for interrupted loading. Subscript "cont" refers to continuous loading and subscript "int" denotes interrupted loading. The probability density function (PDF) of the Weibull distributions describing both groups of data are presented in Fig. 2.15 and characteristic values of cycles to failure are indicated for both distributions. Comparison of the characteristic numbers of cycles (the values of the scale parameters of the two distributions) leads to the conclusion that, as $N_{oint}/N_{ocont} = 1.41$, life is increased by 41% when loading is interrupted.

This comment continues to apply when experimental data are compared, i.e. at a reliability level of 50%. However, when a higher reliability level is desired, e.g.

Fig. 2.15 Probability density function of Weibull distributions describing fatigue data. Characteristic numbers of cycles are shown with vertical lines
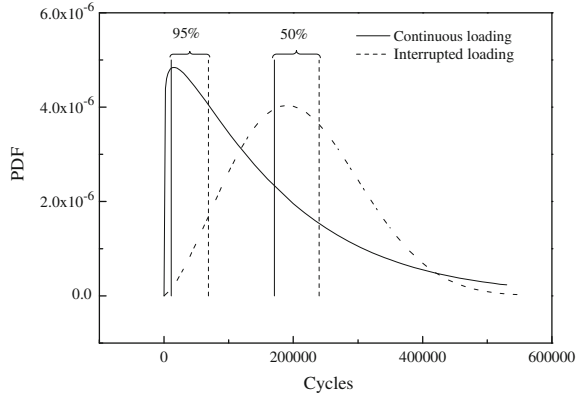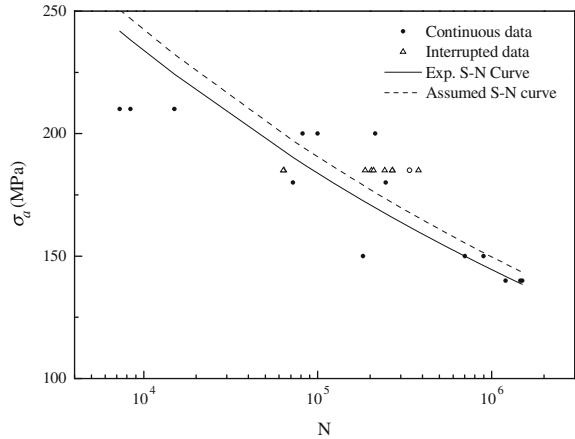

Fig. 2.16 Experimentally derived vs. assumed S-N curve

95%, conclusions are more obvious. In this case, for $P_S(N) = 95\%$, continuously loaded specimens will undergo $N_{cont(95\%)} = 10,914$ cycles prior to failure, while for specimens loaded under interrupted load patterns $N_{int(95\%)} = 68,492$ cycles. Consequently, the ratio of $N_{int(95\%)}$ over $N_{cont(95\%)}$ equals 6.28, meaning that specimen life could be considered as being approximately 630% longer at this reliability level.

It is therefore concluded that material life is longer if loading is interrupted several times during cycling. Therefore, fatigue design allowables, as determined to date, could be far too conservative, and, as demonstrated in Fig. 2.16, curves derived after non-continuous loading could possibly be used for design purposes. Here, the S–N curve determined after continuous testing under $R = 0.1$, at a frequency of 10 Hz, is compared to the hypothetical S–N curve, under interrupted loading at the same stress ratio and frequency conditions. Due to the lack of test data for the derivation of this second curve, it is supposed that it will have the same slope as that determined the conventional way, and it will be shifted to fit test data

under interrupted loading at the maximum stress level of 185 MPa. Therefore, it will be a curve that corresponds to a life 1.4 times longer than that calculated using the experimentally determined S–N curve.

2.2.6 Variable Amplitude Loading

A total of 47 specimens were used for the variable amplitude loading investigation. Specimens cut at 0° and 30°, 60° off-axis directions from the multidirectional laminate were examined experimentally. Two load spectra were used in applying variable amplitude loading on the specimens. For the application of the load, it was decided to keep the frequency constant but not the loading rate in order to obtain data under similar loading conditions to those for CA loading. Constant frequency results in higher loading rates, at high stress levels, while the opposite applies for lower loading levels. However, this is also the case in CA tests, during the determination of an S–N curve. Nevertheless, as has also been reported [28], there is no significant difference in the fatigue life of similar materials to those examined in this study if either constant frequency or constant loading rate is used.

The first applied load sequence is a modified version of a standardized spectrum (WISPERX) that is typically used in the wind turbine rotor blade industry for comparison purposes only in evaluating different materials or life prediction methods for example [29].

WISPERX spectrum is a short version of WISPER (WInd SPEctrum Reference), an irregular time series presented in 1988 [30, 31]. The development of this standardized spectrum was supervised by the IEA (International Energy Association) and a number of European industrial partners and research institutes active in the wind energy domain: FFA, Sweden, NLR and ECN, The Netherlands, Garrad Hassan and Partners and British Aerospace, UK, MAN Technologie GmbH and Germanischer Lloyd, Germany, RISO, Denmark, etc., participated in the working group. The spectrum was based on measurements of bending moment loadings at different sites and for different types of wind turbine rotor blades. A total number of nine different wind turbines with rotor diameters of between 11.7 and 100 m and rotor blades made of different materials such as metals, GFRP, wood and epoxy resins were considered. The WISPER standardized spectrum consists of 132,711 loading cycles, a high percentage of which are of low amplitude. Therefore a long period is needed for the failure of a specimen under this spectrum and for this reason the WISPERX spectrum was derived. It contains approximately 1/10th of the WISPER loading cycles, while theoretically producing the same damage as its parent spectrum. The WISPERX spectrum comprises 12,831 loading cycles since all cycles with a range of below level 17 of WISPER have been removed.

The modified spectrum, henceforth denoted MWX, is in fact a shifted version of the original to produce only tensile loads. The lower positive stress level is the first level of the original time series in which level 25 is considered as zero stress
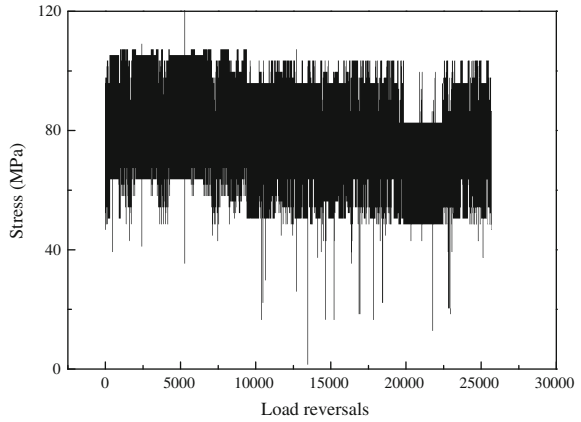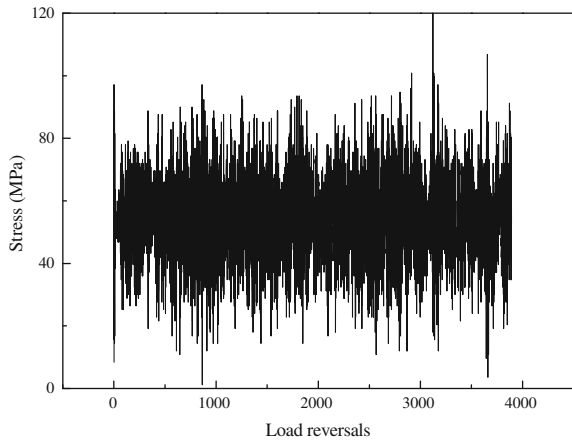
Fig. 2.17 MWX stress time series

Fig. 2.18 EPET573 stress time series

level. The same number of cycles as in the original, 12,831, is maintained. The stress time series for MWX of a maximum applied stress of 120 MPa is presented in Fig. 2.17. This load spectrum was applied on 30 specimens cut at 0°, 30° and 60° from the multidirectional laminate. Fifteen specimens at 0° were tested at three different maximum stress levels, 10 specimens cut at 30° also at three different maximum stress levels, and finally five specimens cut at 60° at two different stress levels. The test frequency was kept constant at 10 Hz and thus the time required from a peak to valley and vice versa was 0.05 s, irrespective of load range.

The second VA series used in the present experimental program was a more realistic spectrum, as it was derived through aeroelastic simulation [32] for a loading case of a 14 m rotor blade [33], and is representative of flap bending moment fluctuations on a cross section of the blade, located 2.4 m from the root. The load case definition [34] is for normal operating conditions at a wind speed of 21 m/s. It represents loading at the current cross-section for 10 min, and contains 3,893 loading reversals, or 1,946 cycles. When the time series is normalized with

Fig. 2.19 Probability distributions of stress ratio values for MWX (*solid line*) and EPET573 (*dashed line*) spectra
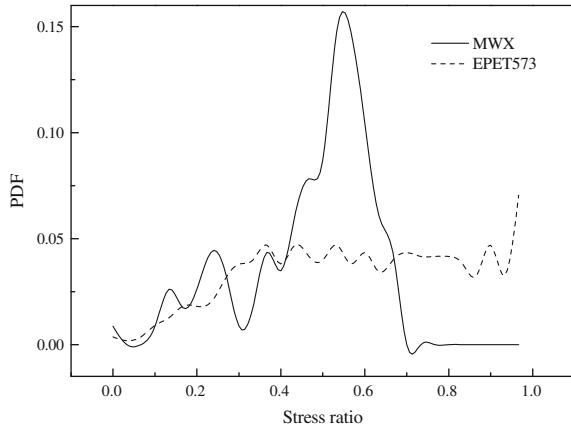
respect to its minimum value and rounded off to integer numbers, it has a maximum value of 157, a minimum of 1, while the mean value is 71.47. The stress time series of this realistic spectrum, henceforth denoted EPET573, for a maximum applied stress of 120 MPa is presented in Fig. 2.18. A total of 17 specimens were tested under EPET573 as follows: eight specimens cut at 0°, tested at two different maximum stress levels, six specimens cut at 30°, tested at three different stress levels and three specimens cut at 60°, tested at one stress level.

Both VA suites are composed of tensile cycles (T-T) of varying stress ratio, R. However, considerable differences are observed regarding the ranges and distribution of R–ratio values for each spectrum. For MWX, the range for R is [0.0516, 0.685] with a mean value of 0.486 and a standard deviation (S.D.) of 0.302, while the respective figures for EPET573 are [0.00345, 0.985], with a mean value of 0.603 and S.D. of 0.402. Probability density functions of R values for both spectra are shown in Fig. 2.19. It is apparent that EPET573 is composed of T-T cycles spanning the range with almost constant density whereas MWX has a much greater density of R values around its mean.

Observation of Figs. 2.17, 2.18 and 2.19 leads to the conclusion that the EPET573 spectrum is much more "irregular" than MWX, which can be considered as a sequence of blocks of almost constant loading patterns. WISPERX and consequently MWX is known by definition to contain mostly cycles of relatively high stress ranges, and has been created for Low Cycle Fatigue (LCF) conditions as it has been extracted from the WISPER spectrum by neglecting cycles of low amplitude. On the other hand, the EPET573 spectrum contains cycles of both high and low amplitudes, as directly derived from aeroelastic simulation. Apparently, even if these two load spectra were applied on a specimen for the same number of cycles at the same maximum applied stress level, MWX is expected to be more damaging than EPET573, which is mainly composed of low range cycles.

The above comments are more easily understood by observing the cumulative spectra of both time series, presented in Fig. 2.20. It is evident that EPET573 is more irregular than MWX, as its cumulative spectrum contains more steps. This is

Fig. 2.20 Cumulative spectra of MWX (*solid line*) and EPET573 (*dashed line*) spectra
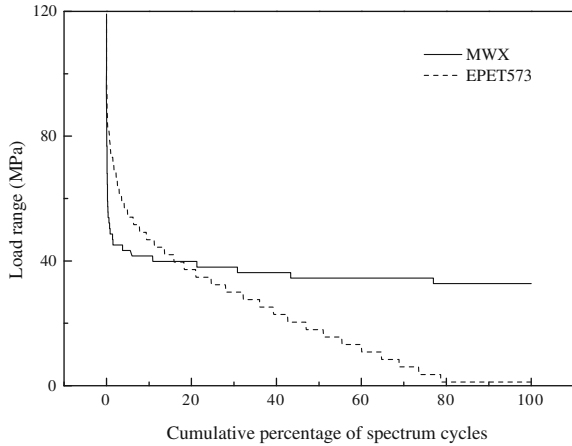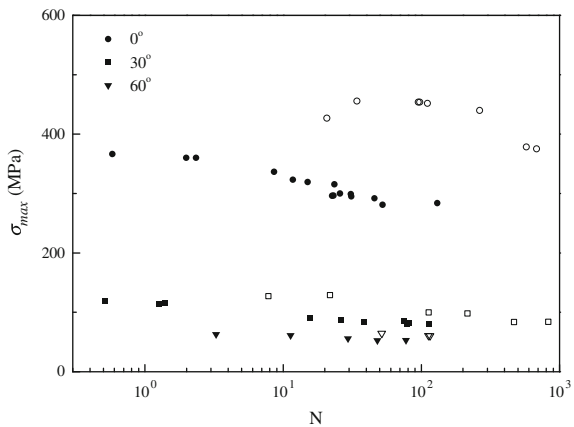

Fig. 2.21 VA experimental results. Closed symbols: MWX, Open symbols: EPET573

reflected in the 553 loading blocks that were used by the rainflow counting routine for the 1,946 counted cycles of the same range and mean values for EPET573, in contrast to only 114 loading blocks used to accommodate the 12,831 counted cycles of the MWX time series. Moreover, in Fig. 2.4 it is shown that MWX has no cycles with a range of less than 30% of its maximum range value, while more than 80% of the counted cycles of EPET573 have ranges below 30% and more than 60% counted cycles have ranges below 15% of the maximum range value.

For both test series, experiments were terminated upon specimen ultimate failure. Results are generally presented with respect to the number of passes of the applied irregular spectrum. Test data are presented in Fig. 2.21 for both MWX and EPET573 spectra, as number of passes vs. maximum applied stress of the VA time series. That is, the initial time series was multiplied each time point by point, by a factor, in order to achieve different levels of loading. This procedure resulted in time series having different mean, minimum and maximum values. The difference

Table 2.8 Experimental results from application of MWX and EPET573 spectra on on– and off–axis specimens

	$\sigma_{\max}$ (MPa)	Cycles to failure	Passes
0ᵒ			
wx1	296.48	296,976	23.15
wx2	300.00	330,360	25.75
wx3	296.30	289,466	22.56
wx4	291.88	586,408	45.70
wx5	299.07	396,222	30.88
wx6	295.16	398,734	31.08
wx7	323.18	151,038	11.77
wx8	366.52	7,505	0.58
wx9	319.41	192,850	15.03
wx10	315.58	301,588	23.50
wx11	281.07	671,640	52.35
wx12	283.83	1,671,388	130.26
wx13	360.00	25,510	1.99
wx14	336.62	110,262	8.59
wx15	360.00	30,033	2.34
ep1	378.21	1,120,744	575.92
ep2	375.16	1,326,439	681.62
ep3	451.92	215,502	110.74
ep4	453.71	185,078	95.11
ep5	455.52	66,584	34.22
ep6	426.94	40,260	20.69
ep7	453.71	189,208	97.23
ep8	439.75	512,938	263.59
30ᵒ			
wx16	79.40	1,012,000	78.87
wx17	90.10	202,008	15.74
wx18	86.64	339,616	26.47
wx19	83.82	495,924	38.65
wx20	114.42	16,172	1.26
wx21	119.35	6,563	0.51
wx22	81.55	1,050,007	81.83
wx23	79.24	1,452,918	113.23
wx24	115.37	17,875	1.39
wx25	86.06	965,482	75.25
ep9	129.03	42,416	21.83
ep10	127.04	15,185	7.82
ep11	99.64	219,642	113.04
ep12	98.18	419,736	216.02
ep13	83.95	1,610,035	828.63
ep14	83.63	911,328	469.03
60ᵒ			
wx26	62.71	41,966	3.27
wx27	60.98	145,026	11.30

Table 2.8 (continued)

	σ_{max} (MPa)	Cycles to failure	Passes
wx28	53.18	992,635	77.36
wx29	55.86	378,151	29.47
wx30	52.67	617,283	48.11
ep15	60.77	218,809	112.61
ep16	64.60	100,380	51.66
ep17	60.30	224,303	115.44

Fig. 2.22 Comparisons of fatigue life of several GFPR materials under WISPERX spectrum
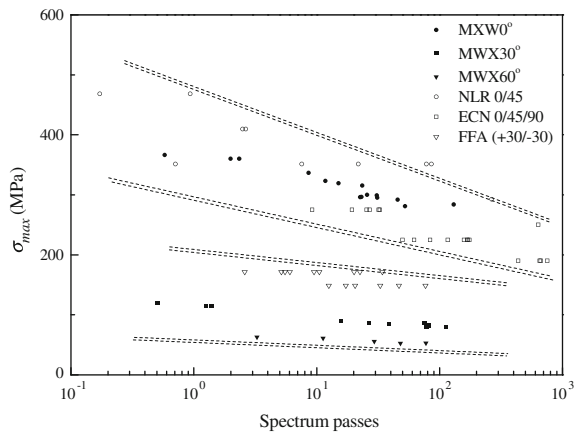
between the two fatigue spectra is well reflected in test results since for the same or even higher maximum stress, specimens tested under the EPET573 spectrum sustain the load for a greater number of passes.

The results of the application of MWX and EPET572 are also tabulated in Table 2.8. The maximum stress presented in Table 2.8 corresponds to the maximum peak of the VA spectrum, while the number of spectrum passes is calculated by dividing the number of cycles by the total number of cycles measured in the spectrum, i.e. 12,831 for MWX and 1,946 for EPT573.

A number of reports referring to experimental results exist [10, 23, 28, 35–37] from the application of the WISPERX spectrum on GFRP laminates. The examined materials were similar to the one examined here and it is therefore possible to compare their fatigue behavior. Such a comparison is shown in Fig. 2.22 for variable amplitude fatigue data collected in different laboratories.

As shown in Fig. 2.22, the variable amplitude fatigue data for the examined similar material can be classified in two scatter bands, depending on whether or not fibers exist along the loading direction. All on-axis specimens exhibit similar fatigue behavior, superior to the corresponding fatigue behavior of the 30° and 60° off-axis specimens.

2.3   Failure of Multidirectional Composite Laminates Under Fatigue Loading

The damage accumulation in composite materials is a multi-parametric phenomenon consisting of a number of different interacting mechanisms that finally lead to material failure. Quantification of the accumulated damage to the material, compared to the virgin version can provide a measure for the life of the examined material if the damage mechanisms can be recognized.

Many researchers have dealt with the measurement of the damage accumulation in fibrous composite materials loaded under static and/or fatigue loading and tried to develop failure criteria based on the measured damage metric. The idea is simple: as more damage is accumulated in the material, the closer it gets to failure. The rate of material deterioration depends on the developed failure mechanisms.

Numerous experimental programs have been performed in order to recognize the damage mechanisms that appear in composite materials and to model their development with fatigue loading. Masters and Reifsneider [38] reported the results of fatigue experiments under tensile loads on CFRP specimens. They measured damage development by interrupting loading periodically and making edge surface replicas. The surface replicas at different stages were then compared to an initial replica that was made, while the specimens were loaded under a 1.1 kN tensile load prior to fatigue testing. They could thus follow the development of the transverse cracks in each layer, and also the interlaminar cracks led to delamination of adjacent plies and ultimate failure. Ferry et al. [39] examined the bending and torsional fatigue behavior of translucent glass/epoxy specimens. A charge-coupled device (CCD) camera that was used to identify the damage development mechanisms recorded microcracks followed by ply delamination and finally fiber fracture. Talreja [3] presented and explained the different failure mechanisms that can develop in different types of fibrous composites and introduced a theory linking the size of each crack in the materials with the macroscopic variation of damage metrics, such as material stiffness.

The results of all the aforementioned theories, together with a number of others in the literature, for example [40–43] lead to the conclusion that the failure mode of a multidirectional laminate under fatigue loading depends mainly on the stacking sequence and loading type. In general, the failure mode under fatigue loads is similar to the failure mode under corresponding quasi-static loading patterns. However, more cracks are accumulated in the matrix of the material with fatigue loading and the type of cracks depends on the cyclic stress amplitude [38, 40]. The accumulation of these cracks results in additional stiffness degradation compared to the quasi-static loading, as reported for example in [40], where for the glass/epoxy examined material the stiffness degradation prior to fatigue failure is approximately 15%, more than double the corresponding stiffness degradation prior to quasi-static failure measured in the range between 3 and 7%.

The main types of damage that can develop during the fatigue failure of a multidirectional laminate can be classified as follows:

- Matrix cracks: Depending on the stress level, these cracks that initially appear in one of the layers can be transferred to adjacent plies under high stress levels, or restricted to the layer in which they initially appeared under low stress levels. These cracks can develop parallel or transverse to the loading [3]. In both cases, depending on the stress level, they can cause delamination or fiber fractures.
- Layer delamination: In many loading cases, the strain field that develops in a multidirectional laminate is such that it does not allow all layers to comply with the strain compatibility equations. In this case, interlaminar stresses develop and lead to delamination of adjacent layers. Subsequently, the layers act independently and not as part of the multidirectional laminate. As stated in [44], the independent layer usually exhibits lower strength than it would as part of the multidirectional laminate.
- Interface failure: The interface is a small region in between the matrix and the fibers where the two components are connected by mechanical and chemical bonds. Crack propagation in this region can be characterized as an interface failure.
- Fiber fracture: This is usually the last stage of damage accumulation in a fibrous composite material. The fibers are the main load-bearing component and their failure is linked to the ultimate material failure as the matrix cannot bear the applied loads without the presence of the fibers. In most cases however, before fiber failure occurs, the matrix is already damaged and unable to transfer any loads.

Although each of the aforementioned failure types can be independently recognized, in practice they act synergistically and appear simultaneously at different locations of the loaded material. Therefore, it is not easy to identify the failure mode of a multidirectional laminate and preferable to characterize one of the many failure modes that appear as the dominant one. The failure mode of a multidirectional laminate is a mixed one containing all the aforementioned types to some extent, depending mainly on stacking sequence and loading type.

These phenomena have been systematically identified and recorded by several means. Methods for the observation of damage initiation and development in composite materials are presented in [38, 41, 42, 45]. Almost all of the non-destructive techniques are also used for the recognition of damage patterns on the surface and also inside composite materials. The most common methods are the following:

- X-rays: With this method it is possible to identify a number of damage types throughout the material volume.
- Acoustic emission: It is known that any type of failure in a material increases the acoustic emission signal. The development of acoustic emission patterns for each failure type and for each material allows the characterization of the damage that causes this failure [45].
- Liquid penetrants and reflected light microscopy [41].
- Surface observation during fatigue loading or post mortem observation using a scanning electron microscope [42].

Fig. 2.23 Stiffness
degradation data for different
material configurations
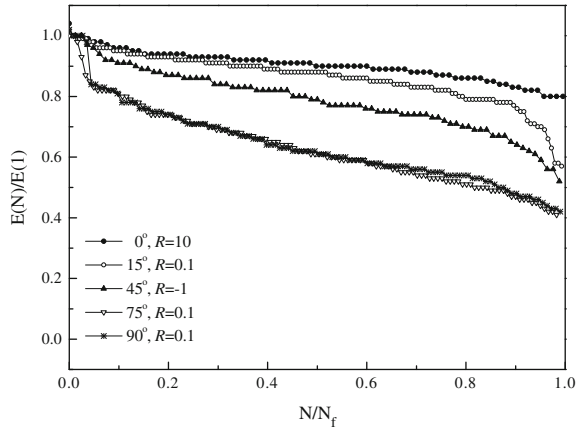
- Ultrasounds, C-scan and D-scan: Ultrasounds can be used for the recognition of damage patterns on the surface or even in the volume of a material.
- Surface replica: A method used in the past, based on the replication of the edge surfaces of the materials during fatigue loading in order to follow damage development, [38, 45].

With all these methods now available, it is relatively easy to recognize the damage mechanisms that are triggered in a composite material during fatigue loading. However, it is difficult to model the interaction of the different mechanisms and predict the consequent material failure.

The results of the experimental program presented in this chapter are consistent with others in the literature. All experimental results lead to the conclusion that the damage mechanism of each failure type for a given composite laminate is strongly dependent on the loading type (tensile or compressive loads) as well as on stress level. Under higher stress levels the failure is more abrupt with less damage accumulation in the material, as was also reported in [7] for a thermoplastic matrix APC-2 material with the stacking sequence $[45/0/-45/90]_{2S}$ loaded under $R = -1$. A result of this is lower decrease in stiffness that is observed when higher stress levels are present. In addition, it has been mentioned that the developed damage mechanisms are also dependent on the stacking sequence of the examined material. A high percentage of fibers along the load direction leads to less damage accumulation during fatigue life and subsequently less stiffness degradation. Photographs of failed specimens are shown below to support these comments.

2.3.1 Stiffness Degradation Measurements

Stiffness degradation was recorded during the constant amplitude fatigue experiment as described above in order to quantify the effect of the fiber orientation, the stress level and the R-ratio on the fatigue failure. The dynamic Young modulus at

the i-th cycle was calculated as being the average slope of data points from the respective hysteresis loop. The latter were recorded continuously for 300 cycles at regular intervals of ca. 10,000 cycles at low stress levels. For higher stresses, the respective interval was 1,000 to 2,000 cycles. Selected results of stiffness degradation measurements are presented in Fig. 2.23 indicating that the variation of this property is related to the off-axis angle and the cyclic stress level.

The data relating to stiffness changes, collected during fatigue experiments on each set of specimens, with a certain R-value and off-axis angle θ, were fitted by a number of probability distributions in order to examine the stochastic behavior of the acquired stiffness degradation data. Five different statistical distributions, namely, the Normal, Log-normal, Weibull, Largest and Smallest element, were selected and fitted to the available experimentally derived stiffness degradation data. The relationships used to define cumulative probability distributions are the following [46]:

Normal:

$$F(x; \mu, \xi) = \int_{-\infty}^{x} \frac{1}{\xi\sqrt{2\pi}} \exp\left[-\frac{(z-\mu)^2}{2\xi^2}\right] dz \tag{2.7}$$

Log-normal:

$$F(x; \mu, \xi) = \int_{-\infty}^{x} \frac{1}{\xi z\sqrt{2\pi}} \exp\left[-\frac{(\ln z - \mu)^2}{2\xi^2}\right] dz \tag{2.8}$$

Weibull:

$$F(x; \eta, \xi) = 1 - \exp\left[-\left(\frac{x}{\xi}\right)^{\eta}\right], x \geq 0 \tag{2.9}$$

Largest element:

$$F(x; \mu, \xi) = \exp\left[-\exp\left(-\frac{x-\mu}{\xi}\right)\right] \tag{2.10}$$

Smallest element:

$$F(x; \mu, \xi) = 1 - \exp\left[-\exp\left(\frac{x-\mu}{\xi}\right)\right] \tag{2.11}$$

It is noted that the symbol ξ is used here instead of the commonly used σ in textbooks to avoid confusing it with stress. The parameters of the distributions for each set of the examined data, based on maximum likelihood estimators, are given in Table 2.9.

The Kolmogorof-Smirnof (K-S) goodness of fit test was performed for each one of the hypotheses. The K-S test results, i.e. the D_N statistic and its probability, $P(D_N)$, for all the aforementioned distributions are given in Table 2.10. Values of

Table 2.9 Stiffness degradation: parameters of various statistical distributions

Angle θ		0		15		30		45		60				75		90		
R-ratio		10	−1	0.1	0.5	0.1	10	−1	10	−1	0.1	0.5	10	−1	0.1	10	−1	0.1
Distribution																		
Normal	μ	0.926	0.941	0.734	0.870	0.897	0.951	0.849	0.932	0.833	0.917	0.889	0.945	0.799	0.685	0.968	0.692	0.926
	ζ	18.79	23.99	5.915	11.63	13.29	26.84	8.868	16.74	8.530	15.14	17.02	23.27	8.970	5.042	27.82	4.904	18.79
Log-normal	μ	0.902	0.919	0.684	0.834	0.862	0.932	0.805	0.904	0.788	0.884	0.866	0.945	0.761	0.632	0.946	0.638	0.902
	ζ	0.050	0.050	0.119	0.085	0.083	0.040	0.104	0.059	0.104	0.079	0.046	0.057	0.080	0.129	0.070	0.129	0.050
Weibull	ζ	0.925	0.942	0.738	0.872	0.900	0.950	0.852	0.931	0.835	0.919	0.886	0.945	0.797	0.690	0.978	0.697	0.925
	η	0.039	0.039	0.094	0.067	0.065	0.031	0.082	0.046	0.082	0.617	0.036	0.036	0.063	0.101	0.055	0.101	0.039
Largest element	μ	−0.104	−0.086	−0.396	−0.188	−0.154	−0.072	−0.226	−0.103	−0.248	−0.128	−0.146	−0.081	−0.278	−0.479	−0.059	−0.469	−0.104
	ζ	0.056	0.056	0.178	0.108	0.104	0.043	0.136	0.066	0.137	0.094	0.053	0.051	0.102	0.201	0.088	0.195	0.056
Smallest element	μ	0.880	0.897	0.630	0.795	0.824	0.914	0.758	0.877	0.741	0.848	0.845	0.903	0.725	0.574	0.914	0.580	0.880
	ζ	0.039	0.039	0.094	0.067	0.065	0.031	0.082	0.046	0.082	0.617	0.036	0.036	0.063	0.101	0.055	0.101	0.039

Table 2.10 K-S test results for the distributions with parameters given in Table 2.9

		Angle θ = 0				15	30		45				60		75	90		
	R-ratio	10	−1	0.1	0.5	0.1	10	−1	10	−1	0.1	0.5	10	−1	0.1	10	−1	0.1
Distribution																		
Normal	D_N	0.113	0.093	0.091	0.103	0.065	0.090	0.069	0.099	0.075	0.108	0.160	0.085	0.108	0.082	0.154	0.107	0.113
	$P(D_N)$	0.250	0.480	0.325	0.130	0.554	0.311	0.883	0.357	0.769	0.121	0.001	0.327	0.181	0.387	0.040	0.139	0.250
Log-normal	D_N	0.088	0.141	0.064	0.115	0.110	0.110	0.048	0.099	0.072	0.159	0.143	0.166	0.087	0.077	0.253	0.104	0.088
	$P(D_N)$	0.549	0.076	0.769	0.069	0.055	0.125	0.997	0.346	0.769	0.005	0.005	0.002	0.419	0.455	0.000	0.160	0.549
Weibull	D_N	0.100	0.103	0.126	0.102	0.049	0.112	0.104	0.113	0.113	0.096	0.213	0.101	0.157	0.144	0.237	0.174	0.100
	$P(D_N)$	0.386	0.343	0.063	0.143	0.872	0.115	0.425	0.206	0.234	0.214	0.000	0.158	0.013	0.012	0.002	0.018	0.386
Largest element	D_N	0.099	0.151	0.069	0.140	0.122	0.113	0.067	0.104	0.091	0.172	0.133	0.078	0.067	0.048	0.274	0.068	0.099
	$P(D_N)$	0.399	0.047	0.679	0.013	0.024	0.109	0.907	0.290	0.486	0.002	0.010	0.438	0.755	0.943	0.000	0.659	0.399
Smallest element	D_N	0.158	0.202	0.098	0.185	0.178	0.153	0.104	0.159	0.136	0.226	0.075	0.129	0.061	0.064	0.322	0.047	0.158
	$P(D_N)$	0.035	0.002	0.244	0.000	0.000	0.010	0.420	0.023	0.090	0.000	0.369	0.031	0.844	0.692	0.000	0.959	0.035

Fig. 2.24 Comparison of experimental and theoretical cumulative distributions of stiffness degradation $R = -1$, 30° off-axis
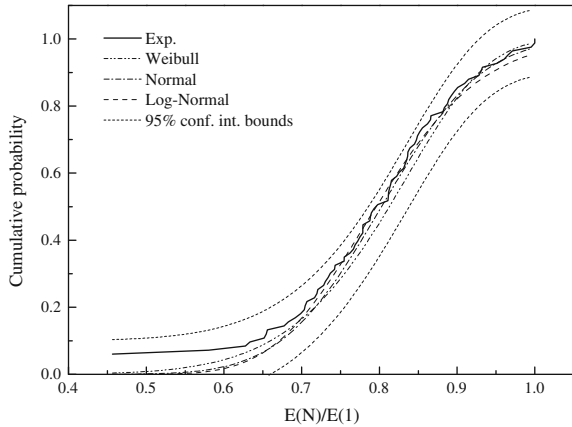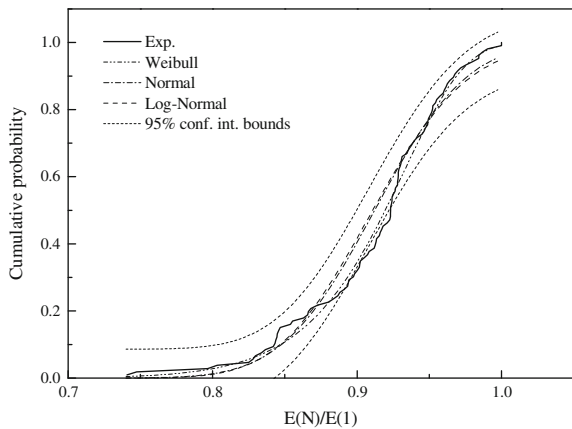

Fig. 2.25 Comparison of experimental and theoretical cumulative distributions of stiffness degradation $R = -1$, 0° on-axis

$P(D_N)$ greater or equal to 0.05 correspond to goodness of fit at a significance level of 5% or higher. The calculation for the K-S test were performed using the method described in [47].

As it is seen from the results in Table 2.10, stiffness degradation data, at a specific R-value and off-axis angle θ, can be modeled by a single statistical distribution for the whole range of stress levels considered for an S–N curve determination. It should be noted that for the cases studied here, the number of experimental points taken into account was at least 80.

An example of favorable and unfavorable comparisons between experimental data and theoretical distributions is given in Figs. 2.24 and 2.25, respectively for different material configurations.

The upper and lower 95% confidence interval bounds correspond to the less satisfactory distribution, which for Fig. 2.24 is the two-parameter Weibull and for

Fig. 2.26 Specimen loaded
on-axis under **a** compression,
$R = 10$, $\sigma_a = 80$ MPa and
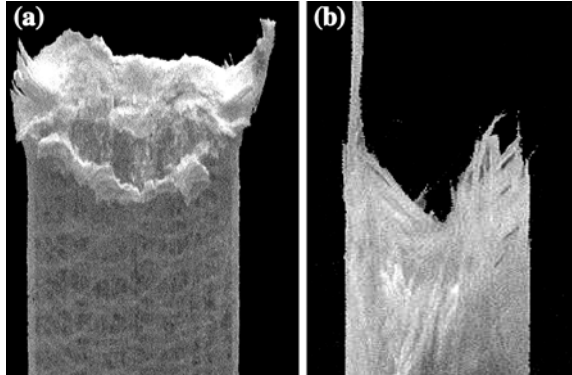**b** tension, $R = 0.1$,
$\sigma_a = 100$ MPa

Fig. 2.25 is the Log-Normal. In this latter case, since the experimental sampling
distribution intersects the 95% confidence bounds, the respective null hypothesis,
i.e. the Log-Normal distribution, is not accepted at the significance level of 5%
[48].

As it can be seen from the results in Table 2.10, the best performing distribution
is the two-parameter Weibull, which succeeds in 14 of the 16 treated cases in
fitting the data at a significance level greater than 5%. The statistical distributions
are sorted according to their fitting capability and therefore, the second best per-
forming function is the Normal. It must be emphasized that in all but one (that of
$R = 10$ at $\theta = 90°$) of the cases treated, stiffness degradation data are satisfac-
torily fitted by a single statistical distribution, at a significance level of 5% or
higher, irrespective of stress level in the same S–N curve.

2.3.2 Dependence on the Loading Type

Application of compressive loads results in less damage accumulation than
application of only tensile loads. This is correlated to fractographic examinations
indicating less matrix cracks in cases of compressive load dominance. A specimen
tested under compression-compression, at stress amplitude of 80 MPa is shown in
Fig. 2.26a while a specimen tested at 100 MPa, under tension-tension loading is
shown respectively in Fig. 2.26b.

Differences in the failed surfaces are obvious. The C-C loaded specimens failed
after local damage accumulation, close to the ultimate fracture region as can be
concluded after inspection of all the failed specimens under these loading condi-
tions. In contrast, when the specimens were tested under tensile loads, detectable
damage is homogeneously distributed throughout the specimen, as fiber splitting
and matrix cracking are present, even in regions far from the separation area. Mean
values of measured stiffness degradation data, prior to failure, from all specimens
tested at specific stress levels and R-ratios follow this trend. As shown in Fig. 2.27,

Fig. 2.27 Stiffness
degradation vs. loading type
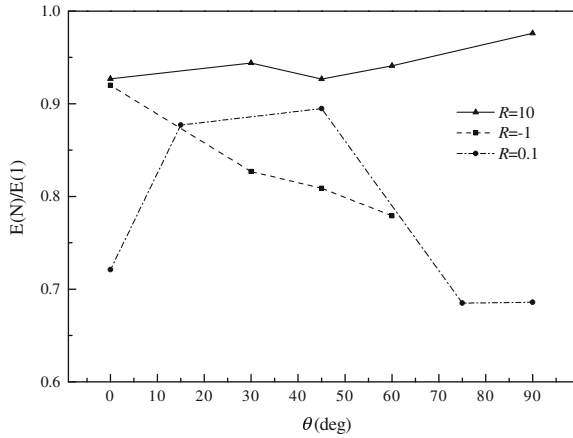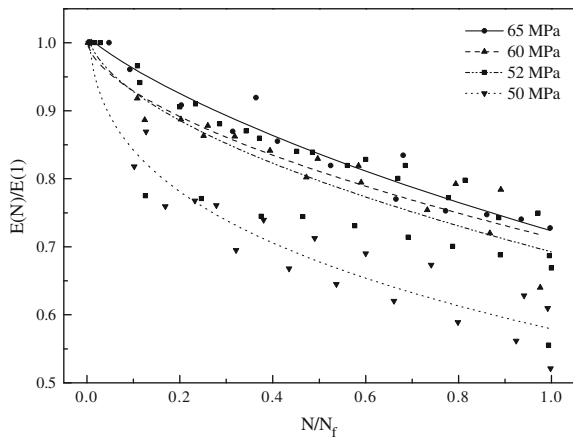and off-axis angle

Fig. 2.28 Stiffness
variations during fatigue life.
Specimens cut at 45°, tested
under $R = -1$

tension-tension and reversed fatigue loading patterns, both containing tensile
loading components, produce significantly higher stiffness degradation than the
compression-compression fatigue, independent of off-axis angle. It is concluded
that tensile loads promote damage accumulation during fatigue life, unlike spec-
imens tested under C-C loads whose elastic modulus seems almost unaffected
during lifetime and changes only just before failure. The behavior of the C-C
loaded specimens can be affected by the used antibuckling device, shown in
Fig. 2.3. The aluminum plates of the antibuckling guide do not allow the specimen
to suffer buckling, but also restrict any out-of-plane deflection that might occur due
to matrix failures. Therefore, it is conjectured that the absence of matrix cracks
during compressive loading may be an artifact due to the use of the antibuckling
guide. It should be mentioned that these failure patterns are representative of all
specimens tested under T-T or C-C loading.

Fig. 2.29 Specimens loaded at 45° off-axis under **a** $R = -1$, $\sigma_a = 60$ MPa and **b** $R = -1$, $\sigma_a = 70$ MPa
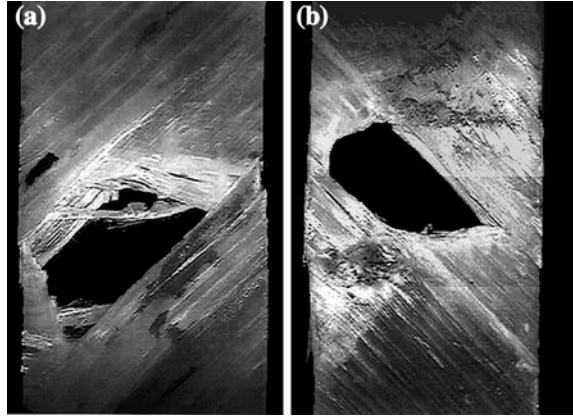
2.3.3 Dependence on the Stress Level

With regard to the effect of the stress amplitude level on the observed modulus reduction, the trend, supported by c.a. 75% of the specimens tested, is that for higher applied cyclic stresses, stiffness degradation is lower. This is derived from measured stiffness degradation data, like those shown in Fig. 2.28 for specimens cut at 45° and tested under $R = -1$.

As shown in Fig. 2.28, the exhibited stiffness degradation follows the afore-mentioned trend. This trend is correlated to fractographic examinations, see for example Fig. 2.29, in which, as mentioned before, the observed higher degree of matrix damage accumulation at lower stress states (specimen on left tested under reversed loading with a maximum cyclic stress of 60 MPa) can be associated with higher stiffness reduction. Nevertheless, failed surfaces of specimens tested at the same stress ratio, R, and off-axis loading orientation, θ, are very similar and it is not easy to distinguish and quantify the net effect of the cyclic stress level based only on their observation.

It must be emphasized however, that when differences in the failure patterns are clearly distinguishable, greater stiffness degradation can occur in the specimens that are more damaged. For example, under reversed loading, $R = -1$, the specimen shown in Fig. 2.29a, tested at the lower stress level, is more damaged than that in Fig. 2.29b, loaded at higher cyclic stresses. More matrix cracks were accumulated in the material in Fig. 2.28a and can be distinguished as white lines parallel to the 45° fibers of the outer layer. Thus, the stiffness degradation exhibited by the specimen in Fig. 2.29a is higher than the corresponding variation in the stiffness in Fig. 2.29b, as shown in Fig. 2.30.

An exception is presented in Fig. 2.31, where, as shown, specimens fatigued on-axis under T-T, $R = 0.1$, do not follow the general trend, i.e. "the higher the stress level, the lower the stiffness degradation". However, it is obvious that the specimen in Fig. 2.31a is more damaged, with evident matrix deterioration before failure although tested under a higher stress level than in Fig. 2.31b. The measured

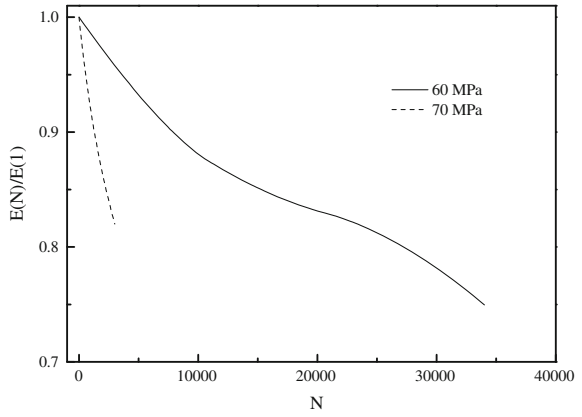**Fig. 2.30** Stiffness degradation of specimens shown in Fig. 2.23

Fig. 2.31 On-axis loaded specimens, **a** $R = 0.1$ $\sigma_a = 80$ MPa, **b** $R = 0.1$, $\sigma_a = 65$ MPa
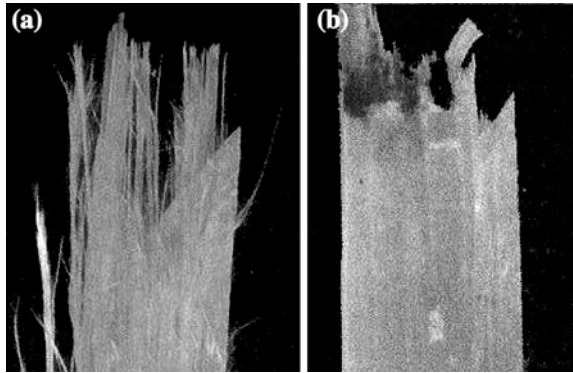

Fig. 2.32 Stiffness degradation measurements for individual specimens cut on-axis
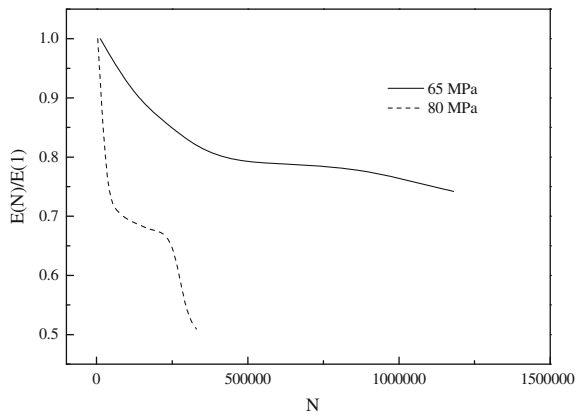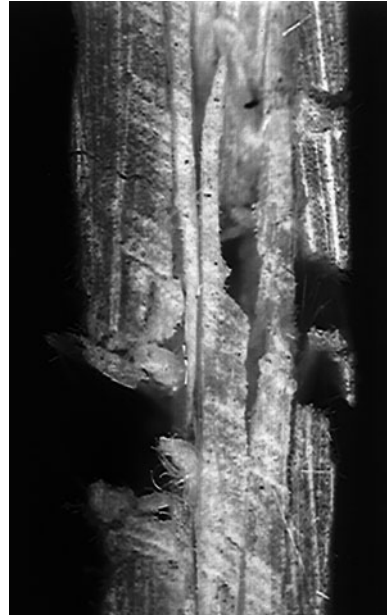
Fig. 2.33 Lateral view of 90° off-axis specimen tested under $R = -1$ at 38 MPa


stiffness degradation for these two specimens (see Fig. 2.32) contradicts the general trend, since the specimen tested under the higher stress level exhibits more stiffness degradation. Nevertheless, the stiffness measurements are in agreement with the observed damage accumulation in the specimens.

2.3.4 Dependence on the Off-Axis Angle

The combined action of in-plane stress tensor components seems to affect stiffness degradation in all cases except the C-C fatigue loading, where, as explained before, the use of the antibuckling device may have masked these effects. For higher off-axis angle specimens, an increased contribution of the transverse normal and the shear stress components to the stress tensor can be calculated and is reflected in higher stiffness degradation values, as shown in Fig. 2.27, where mean values of stiffness degradation data of all specimens, prior to failure, are plotted versus the corresponding off-axis orientation. This is unconditionally valid for reversed loading, whereas for C-C conditions, combined in-plane stress was not found to affect stiffness variations during fatigue life. As far as T-T loading is concerned, results seem to be strongly influenced by the combined in-plane stress, following the aforementioned rule with the exception of specimens cut at 0°, on-axis.

The failure of the off-axis specimens was matrix-dominated, as damage accumulation was characterized by the presence of a multitude of matrix cracks.

Fig. 2.34 Compression-
compression fatigue loading
a on-axis specimen at
$\sigma_a = 70$ MPa, **b** 45° off-axis
specimen at $\sigma_a = 40$ MPa
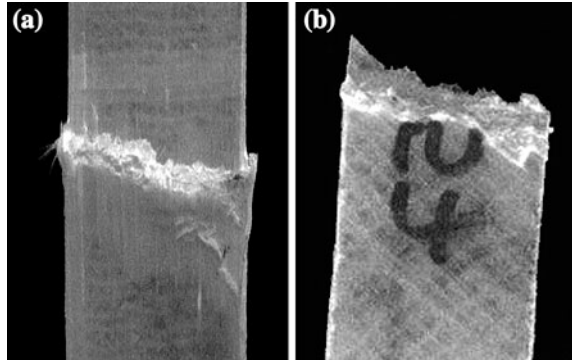
Specimens failed when matrix crack density reached a critical limit. The presence
of a large number of matrix cracks was visually verified for off-axis specimens (see
for example Fig. 2.33, for a 90° off-axis specimen tested under $R = -1$ with a
maximum stress of 38 MPa).

On the other hand, fiber-failure mode was the dominant failure mechanism for
on-axis specimens, regardless of stress ratio. Therefore, failure of specimens
axially loaded along the main fiber direction was more abrupt and fewer stiffness
variations occurred during the fatigue life. In contrast to this rule, specimens tested
under $R = 10$ failed in the same mode, without any visible indication of crack
accumulation away from the failure area, irrespective of the on- or off-axis angle
or cyclic stress amplitude, see Fig. 2.34.

Therefore, the observed stiffness degradation data for these specimens was not
found to depend on the off-axis angle or applied cyclic stress amplitude since, as
measurements showed, it was almost unaffected during lifetime and changed
abruptly just prior to failure.

2.4 Conclusions

The behavior of specimens cut from a multidirectional laminate with the stacking
sequence $[0/(\pm45)_2/0]_T$, typical of that used in several lightweight structures,
loaded under quasi-static and fatigue loading patterns has been examined in this
chapter. The derived database contains 324 fatigue data and 31 quasi-static data.

The experimental results proved that the fatigue strength of the examined
material follows the same trend as its static strength. It is higher in the case of on-
axis specimens and diminishes with the off-axis angle. The unexpected behavior
around the off-axis angle of 45° can be attributed to the stacking sequence of the
laminates. The fibers along the $\pm45^o$ directions are responsible for this increase in
strength when specimens cut at this angle are tested.

The mean stress has been proved to have a significant effect on the fatigue life
of the examined specimens, independent of the off-axis angle. As can be concluded

from the constant life diagrams for the examined on-axis specimens, a Gerber parabola seems more appropriate than the linear Goodman representation. On the other hand, the material seems to be more sensitive to tensile loads only for the low cycle regime. However, experimental results obtained from off-axis specimens proved more resistant against compressive loads.

Another interesting conclusion concerns the interrupted loading results presented. It has been proved experimentally that the load interruptions were beneficial for the fatigue life of the material. Therefore the fatigue failure allowables derived from fatigue tests at high frequencies can be considered as being conservative when they apply to structures that do not operate continuously, such as wind turbine rotor blades, helicopter rotor blades and airplanes.

Fractographic examination of specimens after failure led to useful conclusions regarding damage development and the way in which this damage is related to the loading and the stacking sequence of the examined laminate.

The failure of a multidirectional laminate is a result of the combined effect of a number of interacting phenomena: matrix failure, layer debonding and finally fiber rapture can be observed.

The failure is also related to the loading pattern and is generally different for compressive and tensile loading. However, even when the loading type is the same, the failure mode may be different depending on the stress level. Lower stress levels cause more damage in the material before failure which consequently leads to more stiffness degradation.

The matrix failure and layer delaminations were observed in all failed specimens, especially those loaded under low stress levels. On the other hand, fiber failure is characteristic of higher stress levels and restricted to on-axis specimens, with the exception of the C-C loaded specimens. However, for the examined multidirectional laminates it is not possible to discriminate between pure fiber and matrix failure. Generally speaking, a mixed-mode was observed. Matrix cracks (their number depending on material configuration and loading conditions) developed, followed by layer delaminations and eventually fiber failure.

Investigation of the damage mechanisms shows the way in which damage is accumulated in the material. However, the complexity of these mechanisms and the development of several of them simultaneously, in contrast to metals for example where a single crack is created and leads to material failure, makes it very difficult, if not impossible, to develop a theoretical model that can be based on the fracture mechanics and accurately predict the fatigue behavior of this kind of material. Existing studies, e.g. [3, 49], have proved that the correlation of actual damage mechanisms to easily measured macroscopic quantities for the fatigue life estimation is a very difficult task that can easily lead to erroneous results. It is therefore considered more sensible, especially for design purposes, to adopt fatigue theories based on macroscopic quantities, e.g. cyclic stress and stiffness, for life prediction. Furthermore, the experimental results presented in this chapter for a given glass polyester composite laminate are very similar to others found in the literature for analogous laminates, used in similar engineering

applications. This observation is encouraging for the development of a macro-scopic fatigue failure methodology capable of estimating the fatigue life of composite materials independent of the fiber or matrix type and laminate configuration.

References

1. K.L. Reifsneider, K.N. Lauraitis (eds.), *Fatigue of filamentary composite materials, ASTM STP 636* (American Society for Testing and Materials, Philadelphia, 1977)
2. K.N. Lauraitis (ed.), *Fatigue of Fibrous Composite Materials, ASTM STP 723* (American Society for Testing and Materials, 1981
3. R. Talreja, Fatigue of Composite Materials, Technomic, (1987)
4. P.A. Lagace (ed.), *Composite Material: Fatigue and Fracture, ASTM STP 1012*, vol. 2, (American Society for Testing and Materials, Philadelphia, 1989)
5. K.L. Reifsnider (ed.), *Fatigue of Composite Materials*, Composite Materials Series 4, (Elsevier, Amsterdam, 1991)
6. T.K. O'Brien, Towards a damage tolerance philosophy for composite materials and structures, in *Composite Materials: Testing and Design ASTM STP 1059*, vol. 9, ed. by S.P. Garbo (American Society for Testing and Materials, Philadelphia, 1990)
7. S.G. Pantelakis, T.P. Philippidis, T.B. Kermanidis, Damage accumulation in thermoplastic laminates subjected to reversed cyclic loading. in *High Technology Composites in Modern Applications*, ed. by S.A. Paipetis, A.G. Yioutsos. (University of Patras, Patras 1995) pp. 156–1641
8. C.W. Kensche (ed.), *Fatigue of Materials and Components for Wind Turbine Rotor Blades*, European Commission, Directorate-General XII, Science, Research and Development, EUR 16684, (1996)
9. R.M. Mayer, *Design of Composite Structures Against Fatigue: Applications to Wind Turbine Blades*. (Antony Rowe Ltd., Chippenham, Wiltshire, 1996)
10. B.J. de Smet, P.W. Bach, Database fact: fatigue of composites for wind turbines, ECN-C-94-045, (1994)
11. J.F. Mandell, D.D. Samborsky, DOE/MSU Composite Material Fatigue Database. Sandia National Laboratories, SAND97-3002, online via www.sandia.gov/wind, v. 18, 21st March Updated (2008)
12. D.R.V. van Delft, H.D. Rink, P.A. Joosse, P.W. Bach, Fatigue behaviour of fibreglass wind turbine blade material at the very high cycle range. in *European Wind Energy Conference Proceedings*, vol. 1. (Thessaloniki, Greece, 1994) pp. 379–384
13. A.T. Echtermeyer, Fatigue of glass reinforced composites described by one standard fatigue lifetime curve. In *European Wind Energy Conference Proceedings*, vol. 1 (Thessaloniki, Greece, 1994) pp. 391–396
14. P.A. Joosse, D.R.V. van Delft, P.W. Bach, Fatigue design curves compared to test data of fibreglass blade material, in *European Wind Energy Conference Proceedings*, vol. 3, (Thessaloniki, Greece, 1994) pp. 720–726
15. C.W. Kensche, Lifetime of gl-ep rotor blade material under impact and moisture, 3rd Symposium on Wind Turbine Fatigue Proceedings, Petten, Holland: IEA, April 21–22, (1994) pp. 137–143
16. D.R.V. van Delft, G.D. de Winkel, P.A. Joosse, Fatigue behavior of fiberglas wind turbine blade material under variable loading, *4th Symposium on Wind Turbine Fatigue Proceedings*, Stuttgart, Germany: IEA, Feb 1–2, (1996) pp. 75–80
17. C.W. Kensche. Which slope for GL-Ep fatigue curve? *4th Symposium on Wind Turbine Fatigue Proceedings*, Stuttgart, Germany: IEA, Feb 1–2, (1996) pp. 81–85

18. M.J. Owen, G.R. Griffiths, Evaluation of biaxial stress failure surfaces for a glass fabric reinforced polyester resin under static and fatigue loading. J. Mater. Sci. **13**(7), 1521–1537 (1978)
19. Toru. Fujii, Fan. Lin, Fatigue behavior of a plain-woven glass fabric laminate under tension/torsion biaxial loading. J. Compos. Mater. **29**(5), 573–590 (1995)
20. T.P. Philippidis, A.P. Vassilopoulos, Fatigue strength prediction under multiaxial stress. J. Compos. Mater. **33**(17), 1578–1599 (1999)
21. T.P. Philippidis, A.P. Vassilopoulos, Fatigue of composite laminates under off-axis loading. Int. J. Fatigue **21**(3), 253–262 (1999)
22. T.P. Philippidis, A.P. Vassilopoulos, Fatigue design allowables of grp laminates based on stiffness degradation measurements. Compos. Sci. Technol. **60**(15), 2819–2828 (2000)
23. S.I. Andersen, P.W. Bach, W.J.A. Bonee, C.W. Kensche, H Lilholt, A. Lystrup, W. Sys, *Fatigue of Materials and Components for Wind Turbine Rotor Blades*, ed. by C.W. Kensce, Directorate-General XII, Science, Research and Development, EU-16684 EN, (1996)
24. S.W. Tsai, H.T. Hahn, Introduction to Composite Materials. Technomic (1980)
25. P.W. Bach, Glass and hybrid fibre performance. in *Design of Composite Structures Against Fatigue. Applications to Wind Turbine Blades*, ed. by R. M. Mayer (Antony Rowe Ltd., Chippenham, Wiltshire, 1996)
26. B. Harris, N. Gathercole, H. Reiter, T. Adam, Fatigue of carbon-fibre-reinforced plastics under block-loading conditions. Compos. Part A Appl. Sci. **28**(4), 327–337 (1997)
27. M. Ansell, I. Bond, P. Bonfield, C. Hacker, Fatigue properties of wood composites. in *Design of Composite Structures Against Fatigue. Applications to Wind Turbine Blades*, ed. by R.M. Mayer (Antony Rowe Ltd., Chippenham, Wiltshire, 1996)
28. C.W. Kensche, *GFRP Fatigue Data for Certification. European Wind Energy Conference Proceedings,* vol. I, (Thessaloniki, Greece, 1994) pp. 738–742
29. T.P. Philippidis, A.P. Vassilopoulos, Life prediction methodology for GFRP laminates under spectrum loading. Compos Part A–Appl S **35**(6), 657–666 (2004)
30. A.A. Ten Have, Wisper: Introducing variable-amplitude loading in wind turbine research. *The 10th BWEA Conference*, London, UK, Mar 23–25 (1988)
31. A.A. Ten Have. Wisper: A standardized fatigue load sequence for HAWT-blades. European Community Wind Energy Conference proceedings, Henring Denmark, June 6–10, (1988) pp. 448–452
32. V.A. Riziotis, S.G. Voutsinas, Fatigue loads on wind turbines of different control strategies operating in complex terrain. J. Wind. Eng. Ind. Aerod. **85**(3), 211–240 (2000)
33. T.P. Philippidis, D.J. Lekou, A.P. Vassilopoulos, EPET II #573, University of Patras, First Semester Progress Report, (in Greek) (1997)
34. Draft IEC 61400-1, Ed.2 (88/98/FDIS): Wind turbine generator systems–Part 1: Safety requirements, (1998)
35. P.W. Bach, P.A. Joose, D.R.V. van Delft. Fatigue lifetime of glass/polyester laminates for wind turbines. *In the European Wind Energy Conference Proceedings,* vol. I, (Thessaloniki, Greece, 1994) pp. 94–99
36. M. Poppen, P. Bach, Influence of spectral loading. in *Design of Composite Structures Against Fatigue. Applications to Wind Turbine Blades*, ed. by R.M. Mayer (1996)
37. R.P.L. Nijssen, OptiDAT–fatigue of wind turbine materials database, 2006. http://www.kc-wmc.nl/optimat_blades/index.htm
38. J.E. Masters, K.L. Reifsneider, An investigation of cumulative damage development in quasi-isotropic graphite/epoxy laminates. in *Damage in composite Materials, ASTM STP 775*, ed. by K.L. Reifsneider, American Society for Testing and Materials (1982) pp. 40–62
39. L. Ferry, D. Rerreux, D. Varchon, N. Sicot, Fatigue behaviour of composite bars subjected to bending and torsion. Compos. Sci. Technol. **59**(4), 575–582 (1999)
40. G. Caprino, G. Giorleo, Fatigue lifetime of glass fabric/epoxy composites. Compos. Part A Appl. Sci. **30**(3), 299–304 (1999)

41. F. Gao, L. Boniface, S.L. Ogin, P.A. Smith, R.P. Greaves, Damage accumulation in woven fabric laminates under tensile loading: Part I. Observations of damage accumulation. Compos. Sci. Technol. **59**(1), 123–136 (1999)
42. E.K. Gamstedt, L.A. Berglund, T. Peijs, Fatigue mechanisms in unidirectional glass-fibre-reinforced polypropylene. Compos. Sci. Technol. **59**(5), 759–768 (1999)
43. M.M. Ratwani, H.P. Kan, Effect of stacking sequence on damage propagation and failure modes in composite laminates. in *Damage in composite materials, ASTM STP 775*, ed. by K.L. Reifsneider, (American Society fot Testing and Materials, 1982) pp. 40–62
44. A. Rotem, Prediction of laminate failure with the rotem failure criterion. Compos. Sci. Technol. **58**(7), 1083–1094 (1998)
45. T.P. Philippidis, V.N. Nikolaidis, J.G. kolaxis, Unsupervised pattern recognition techniques for the prediction of composite failure. J. Acoust. Emission. **17**(1–2), 69–81 (1999)
46. G.J. Hahn, S.S. Shapiro, *Statistical Models in Engineering* (Wiley, New York, 1994)
47. W.H. Press, S.A. Teukolsky, W.T. Vetterling, B.P. Flannery, in *Numerical Recipes in Fortran. The Art of Scientific Computing*, 2nd edn. (Cambridge University Press, Cambridge, MA, 1994)
48. F.J. Massey, The Kolmogorov-Smirnof test for goodness of fit. J. Am. Stat. Assoc. **46**, 68–78 (1951)
49. G.P. Sendeckyj, Life prediction for resin-matrix composite materials. in *Fatigue of Composite Materials*, Composite Materials Series 4, ed. by K.L. Reifsnider (Elsevier, Amsterdam, 1991)